

MR. HUGO JAKE UVEGI (Orcid ID : 0000-0002-2846-6078)

Article type : Article

Reactivity of industrial wastes as measured through ICP-OES: A case study on siliceous Indian biomass ash

Hugo Uvegi¹, Piyush Chaunsali², Brian Traynor¹, Elsa Olivetti^{1*}

¹Department of Materials Science and Engineering, MIT, Cambridge, USA 02139

²Department of Civil Engineering, IIT Madras, Chennai, India 600036

Hugo Uvegi (huvegi@mit.edu)

Piyush Chaunsali (pchaunsali@iitm.ac.in)

Brian Traynor (btraynor@mit.edu)

Elsa Olivetti (elsao@mit.edu), +16172530877

Abstract

An untapped source of amorphous SiO₂, industrially generated Indian biomass ash (SA)—90% amorphous, with composition of ~60% SiO₂ and ~20% unburnt carbon—can be used to produce cementitious and alkali activated binders. This study reports dissolution of amorphous Si from SA in 0.5 M and 1 M aqueous NaOH, with and without added Ca(OH)₂, at SA:Ca(OH)₂ wt% ratios of 100:0, 87.5:12.5, and 82.5:17.5. Monitoring of elemental dissolution and

This is the author manuscript accepted for publication and has undergone full peer review but has not been through the copyediting, typesetting, pagination and proofreading process, which may lead to differences between this version and the [Version of Record](#). Please cite this article as [doi: 10.1111/JACE.16628](https://doi.org/10.1111/JACE.16628)

This article is protected by copyright. All rights reserved

subsequent/simultaneous product uptake by ICP-OES offers an effective process for evaluating utility of industrial wastes in binder-based systems. After 28 days in solution, up to 68% of total Si is dissolved from SA in 1 M NaOH, with values as much as 38% lower in the presence of $\text{Ca}(\text{OH})_2$, due to the formation of tobermorite-like C-S-H. FTIR, ^{29}Si MAS-NMR, and XRD are used to characterize solid reaction products and observe reaction progress. Product chemistries calculated from ICP-OES results and verified by selective dissolution in EDTA/NaOH—namely, Ca/Si of 0.6-1 and Na adsorption of 1-2 mmol/g—are found to be consistent with those indicated by aforementioned techniques. This indicates the efficacy of ICP-OES in estimating product chemistry via such a methodology.

1. Introduction

Direct emissions and fuel consumption associated with ordinary Portland cement (OPC) production is responsible for most of the estimated 5-8% of global annual CO_2 emissions attributed to concrete.^{1,2} Alkali activated materials and geopolymers offer cement-free alternatives with comparable physical properties,^{3,4} and regular use of industrial byproducts as precursors suggests substantially lower environmental footprints.^{5,6} Still, as researchers expand their search for useful precursors, it is becoming increasingly apparent that any byproduct stream must be of adequate scale to offset demand for binder-based building materials.^{6,7} Effective reduction of environmental impacts therefore necessitates a systems approach, including analysis of both byproduct supply relative to local binder demand as well as material chemistry and reactivity in activating solutions. In this work, we propose a multi-faceted approach to characterizing elemental availability and reactivity through a focused investigation of siliceous Indian biomass ash (SA).

SA is sourced from a paper mill in northern India, which utilizes rice husk and sugarcane bagasse as primary incineration feedstocks. With global annual rice paddy and sugarcane production at 760 million and 1.8 billion tonnes,^{8,9} respectively, their residues, husks (~20 wt% of rice paddy¹⁰) and bagasse (~30 wt% of sugarcane⁹), are similarly abundant and often burned

as fuel by small and medium-scale enterprises in developing countries. Like other stalky and husk-protected plant-matter, these residues are rich in silica,^{11,12} the chemical availability of which depends on incineration conditions.^{12–14} While biomass incineration is increasingly hailed as a sustainable alternative to fossil fuel combustion,¹⁵ current practices yield multi-ton daily landfill burdens. Extraction of reactive silica from such ashes for use in binder synthesis provides an upcycling opportunity as described previously,¹⁶ both reducing environmental footprint and adding economic benefit for industrial plant owners. It is important to note that regional and seasonal crop variability results in fluctuations in residue ash composition,^{17,18} thereby influencing utility. Still, while global supply of these byproducts are surely lower than current global OPC production,¹⁹ given the heterogeneous distribution of such byproduct supply, it is important to investigate for their potential to offset local demand for OPC near byproduct production sites.

To this end, we offer a detailed physicochemical analysis of SA, its dissolution in aqueous sodium hydroxide (NaOH) solutions, and its reaction with calcium hydroxide ($\text{Ca}(\text{OH})_2$) in such aqueous solutions, forming an alkali-activated tobermorite-like calcium silicate hydrate (C-S-H) product with minimal alkali incorporation.

Following prior work by the authors on mix design,²⁰ mineralogical characterization,¹⁶ and leaching characteristics²¹ of SA-based masonry, in this study, we characterize reaction progress and elemental inclusion into products through a multi-faceted characterization approach, centered on analysis of inductively coupled plasma optical emission spectroscopy (ICP-OES) results. We compare SA dissolution in aqueous NaOH with results from similar dissolution in the presence of added $\text{Ca}(\text{OH})_2$. By quantifying differences in the presence of relevant elemental species (e.g. Si, Ca, and Na) between the ash and ash/lime systems, we deduce product chemistry. This chemistry is compared with results from selective dissolution in salicylic acid/methanol and EDTA/NaOH solutions, as described previously in the literature.²² X-ray diffraction and spectroscopic analysis of solids further confirm precursor and product chemistry and structure, resolving amorphous and crystalline phase distribution as well as elemental

bonding environments. Through a combined analysis we quantify the extent of silica dissolution and incorporation, C-S-H type, Ca/Si ratio, adsorption of sodium from the activating solution, and mean chain length.

Silica dissolution, vital to geological processes and cementitious systems alike, has been the focus of much research over the past decades. Iler's pivotal 1979 book²³ reviewed the state of the art of silica science, devoting a significant portion to the dissolution and solubility of both crystalline and amorphous silica. As discussed by Iler, and as observed before and since, amorphous silica displays significant solubility in alkaline media, due to the acidity of typically hydroxylated surface species as well as the propensity for hydrolysis of non-equilibrium Si-O bonds in alkaline environments, yielding the formation of silicate ions in addition to the orthosilicic acid monomers present during dissolution in water.²³⁻²⁷ The situation becomes more complicated in the presence of other polyvalent metal oxides, such as is the case with most supplementary and alternative cementitious materials.²⁷⁻³²

Recently, Kim and Olek (2014),³³ Maraghechi, et al. (2016),³⁴ and Noguchi, et al. (2018)³⁵ observed the dissolution of reactive silica, as α -cristobalite, silicate glass, and Pyrex glass, respectively, in aqueous alkali hydroxide solutions of various pH and Ca^{2+} concentrations. These and other works^{36,37} focus primarily on implications for the alkali-silica reaction in concrete. Still, they provide important ground-work for developing similar methodologies for investigating reactivity of aluminous and siliceous byproduct materials.

Xu and van Deventer (2000)³⁸ studied relationships between crystalline aluminosilicate minerals, activator concentration, and geopolymerization potential, noting that minerals which exhibit higher dissolution extents typically yield binder products with stronger compressive strengths. Hajimohammadi and van Deventer (2016)³⁹ studied the dissolution kinetics of a range of more reactive, predominantly amorphous precursor aluminosilicate materials for use in geopolymeric systems and the effect of milling time and particle size on dissolution kinetics. The amorphous materials studied in the latter work exhibited significantly higher levels of

dissolution. Abreu, et al. (2005)⁴⁰ studied the hydration of rice husk ash through ²⁹Si MAS-NMR spectroscopy, while Heo, et al. (2015)⁴¹ investigated the use of pure rice husk ash as a substitute for fumed silica in the synthesis of water glass (i.e. sodium silicate solution) for use in geopolymer synthesis. Biernacki, et al. (2001)⁴² investigated the consumption of Ca(OH)₂ during the pozzolanic reaction with Class F fly ash, going one step further to quantify the associated reaction kinetics. All observed the rapid reaction of amorphous silica found in the ash.

Inspired by these works, this study centers on the use of ICP-OES in conjunction with other techniques to quantify both dissolution and uptake of reactive elements in precipitate species. Using this approach as a basis for material reactivity allows for extrapolation of material utility in large-scale operations.

2. Experimental Program

2.1. Materials

The precursor of focus in this study is an Indian biomass ash (SA), sourced from Silverton Pulp & Papers Pvt. Ltd. in Muzaffarnagar, Uttar Pradesh, India, and derived from the incineration of a feedstock composed primarily of rice husk and sugarcane bagasse residues. The oxide composition was determined by XRF using ASTM C311 and is presented in Table 1.

Note the high SiO₂ and loss on ignition (LOI) values in the ash. Such high LOI indicates the presence of significant unburnt organic material in the ash, primarily due to boiler inefficiencies at the Silverton plant. While often used as a proxy for unburnt carbon (UC), LOI has recently been shown to overestimate such values.⁴³ Two-atmosphere thermogravimetric analysis as described by Mohebbi, et al. (2017) quantifies UC content in SA at 20-22%. While implications of UC are outside the scope of this paper, this demonstrates that while LOI is indicative of UC content in carbonaceous systems, further analysis is necessary for exact quantification.

The highly amorphous nature of the ash is evidenced by the hump centered at ~22° 2θ in the X-ray diffraction pattern in Figure 1(a). Amorphous content and phase composition of the ash was determined previously by quantitative Rietveld refinement as described in the Methods

section.¹⁶ The ash was found to be ~90% amorphous, including the contribution from residual carbon. Figure 1(b) depicts XRD patterns from three different fractions of ash: <45 μm , 45-150 μm , and 150-500 μm , which previous work²⁰ showed to comprise ~23%, ~56%, and ~21% of the ash, respectively, as determined by particle size analysis. All samples were ground and passed through a 325 no. (45 μm) sieve prior to analysis.

2.2. Methods

2.2.1. Sample Production

Dissolution experiments were prepared in Reagent grade water, 0.5 mol/L (M) and 1 M aqueous NaOH solutions (ACS Reagent grade water, RICCA Chemical Company; NaOH $\geq 97\%$, Sigma Aldrich) at a constant liquid/solid (L/S) ratio of 25 (i.e. 2 grams of solid in 50 mL of solution). Reaction experiments were carried out in similar solutions, with the addition of hydrated lime ($\text{Ca}(\text{OH})_2 \geq 98\%$, Macron Fine Chemicals) in two lime/ash ratios (i.e. 12.5 and 17.5 wt% $\text{Ca}(\text{OH})_2$ at the same L/S). The lower ratio was chosen to mimic the Ca/Si ratio explored in previous works by a subset of the authors,^{16,20,21} while the higher ratio was chosen to explore the effect of elevated Ca/Si.

Samples were mixed continuously in a tube rotator (Fisherbrand™ Multi-Purpose Tube Rotator, Fisher Scientific) to ages of 6, 24, 72, 168, 336, and 672 hours (0.25, 1, 3, 7, 14, and 28 days, respectively) to explore dissolution and reaction kinetics. Dilute environments and continuous mixing were employed to disrupt the formation of strong concentration gradients near dissolving solid surfaces and maximize diffusivity of reactive species, thereby creating an environment in which dissolution and precipitation could be assumed to be surface-limited.

At each age, samples were vacuum filtered through a 0.2 μm membrane (Pall membrane, VWR), and filtrates were retained for subsequent ICP-OES analysis. Solids were immersed in isopropyl alcohol for 24 hours to stop hydration, filtered through 2.5 μm filter paper (Quantitative filter paper, ashless, Grade 42, Whatman) for solid retention, dried at 40 $^\circ\text{C}$ for 3 hours, and finally stored in a vacuum desiccator to minimize carbonation. Samples are

identified by solution molarity, age (in hours), solid ingredients (S = Silverton Ash, L = 12.5% $\text{Ca}(\text{OH})_2$, LH = 17.5% $\text{Ca}(\text{OH})_2$), as shown in Table 2. All samples were prepared in triplicate.

2.2.2. Inductively coupled plasma optical emission spectrometry (ICP-OES)

An Agilent 5100 Vertical Dual View ICP-OES with auto-sampler was used to analyze reactant dissolution. Calibration standards ranging from 0.1 to 200 mg/L were prepared from two standard solutions—1000 mg/L Si in H_2O and 1000 mg/L each of Ca, Al, Na, K, Mg, Fe, and S in 4 wt% HNO_3 (Elemental Scientific, Omaha, NE)—using 2 wt% HNO_3 solution (prepared from TraceSELECT concentrated HNO_3 and ACS reagent grade water) for dilution. Reagent Grade water, 0.5 M, and 1 M samples were diluted in the same 2 wt% HNO_3 solution at sample/diluent ratios of 1:10 and 1:200 (i.e. 1 mL and 0.05 mL of sample in 10 mL of 2 wt% HNO_3 , respectively) to effectively measure concentrations of dilute and concentrated elements in solution, respectively. Dissolution extents of relevant elements are calculated by comparison of ICP-OES results with total elemental percentage as derived from XRF data.

2.2.3. X-ray diffraction (XRD)

Mineralogical phase distributions of raw materials and hydrated samples were determined using X-ray diffraction. XRD data was collected using high speed Bragg-Brentano optics on a PANalytical X'Pert Pro MPD operated at 45 kV and 40 mA. Data was obtained between 5° and 70° (2θ) using a step size of 0.0167° with each sample scan lasting 52 minutes. The diffractometer was configured with a $1/2^\circ$ divergent slit, a 0.04 radian sollar slit, and a 1° anti-scatter slit. The powdered sample was packed into a 27 mm diameter sample holder. HighScore Plus software was used for quantitative X-ray diffraction.

2.2.4. Fourier transform infrared spectroscopy (FTIR)

FTIR Spectroscopy was performed using a Thermo Scientific Nicolet 6700 Fourier Transform Infrared Spectrometer. Transmission spectra were collected from 4000 to 400 cm^{-1} with a resolution of 2 cm^{-1} . Spectra were averaged over 32 scans. Samples were run using the KBr pellet method, with approximately 1 mg of sample blended with 400 mg of KBr (Ultra High Purity, International Crystal Laboratories) matrix immediately prior to measurement.

2.2.5. ^{29}Si Magic Angle Spinning Nuclear Magnetic Resonance Spectroscopy (^{29}Si MAS-NMR)

²⁹Si MAS-NMR spectra were obtained at room temperature on a Bruker Avance III WB 500 MHz spectrometer (field strength of 11.74 T) equipped with a 4.0 mm 2-channel broadband HX solid state probe. Spectra were obtained in single-pulse experiments, with the spectrometer tuned to 99.325 MHz, a spinning speed of 10 kHz, 20 s relaxation delays, up to 3400 scans, a ²⁹Si $\pi/2$ pulse of 4 μ s, with 49 kHz of ¹H spinal-64 decoupling applied during acquisition. ²⁹Si chemical shifts were referenced externally to hexamethylcyclotrisiloxane at -9.00 ppm. ²⁹Si resonances were analyzed according to Q^n classification, where n corresponds to the connectivity of silicate tetrahedra and can vary from 1 to 4. Q^2 can be further classified as either Q^2_b or Q^2_p , where b and p respectively refer to bridging and pairing silicate tetrahedra in the drierketten structure of C-S-H. To carry this out, spectra were deconvoluted using MestReNova software, maintaining a Gaussian peak shape and a Q^2_p/Q^2_b ratio equal to 2, consistent with the drierketten structure.

2.2.6 Selective Dissolution

To verify reaction product chemistry, two selective dissolution techniques were used—salicylic acid/methanol (SAM) and ethylenediaminetetraacetic acid/sodium hydroxide (EDTA/NaOH) extractions, as described by Ben Haha, *et al.* (2010).²² Further description is provided in supplementary information and Table S4.

3. Results

Given the chemistry and amorphous nature of as-received SA, as well as the experimental setup, dissolution of Si from SA was expected to proceed quickly.⁴⁴ This is confirmed in Figure 2(a): while water was ineffective at dissolving Si, 0.5 M and 1 M aqueous NaOH solutions yielded Si dissolution following an asymptotic trend. These solutions achieved 672-hour dissolution extents of <1%, 51-53%, and 67-68% of total Si in ash for water (0S), 0.5 M (0.5S), and 1 M (1S) NaOH solutions, respectively. These numbers increase slightly when accounting for the fact that only ~90% of Si is contained in an amorphous phase; other Si-containing phases in SA include quartz, cristobalite, and albite,¹⁶ which are not expected to react under presented experimental conditions. All final Si concentrations are below respective solubility limits.^{23,24,45}

Figure 2(a) further presents 0.5 M and 1 M dissolution experiments in the presence of added $\text{Ca}(\text{OH})_2$ (0.5SL, 0.5SLH, 1SL, and 1SLH). Unlike the purely ash systems, these solutions exhibited two distinct dissolution regimes—(1) an early-age regime seemingly lacking Si dissolution (i.e. no Si present in solution), followed by (2) a later-age regime in which the familiar asymptotic trend is observed. The duration of regime (1) is observed to be system-dependent, exhibiting timespans of <72 hours for 1SL, <168 hours for 0.5SL and 1SLH (0.5SL appears to exit regime (1) before 1SLH), and <336 hours for 0.5SLH. Although qualitative, dashed curves for the ash/lime systems are presented to guide the reader's eye, and time points at which regime (1) end are estimated with kinks in the curve. SL and SLH systems tended towards 37-43% and 20-32% Si dissolution, respectively. Lime-containing studies carried out in water are not presented, as the addition of lime did not significantly influence dissolution. As compared to respective ash systems absent of lime, these numbers represent ~12-38% decreases in apparent Si dissolution. Spectroscopic results described below indicate the precipitation of a C-S-H reaction product, providing reasonable explanation as to the cause of the flat regime, and thus, this decrease in apparent dissolution. Aluminum data is not presented here since it was minimally present in both the raw ash (see Table 1) and in solution post-dissolution.

Figure 2(b) is included as further evidence that SA dissolution is mainly a result of amorphous Si decomposition (similar results for different ash fractions are included in Figure SI1). Comparison of the different ash fractions in Figure 1(b) suggests the presence of two distinct contributions to the amorphous hump—one due to a silica-rich amorphous phase yielding a broad peak centered at $\sim 22^\circ 2\theta$,²⁹ and the other due to the presence of activated/amorphous carbon yielding a broad peak centered at $\sim 25^\circ 2\theta$ ⁴⁶ (corresponding to relatively longer bond lengths in amorphous Si-O than in amorphous carbon). More prevalent in larger ash fractions, the presence of activated carbon can be explained by inefficient combustion and evidenced by high LOI (LOI of each ash fraction is included in Table SI1). In Figure 2(b), we compare XRD patterns of the largest ash fraction before and after 28 days of dissolution, confirming that the residual amorphous hump is predominantly due to the continued presence of amorphous carbon. ICP-OES results (i.e. comparison of carbon line intensities between blank and ash samples) and

previous literature⁴⁷ indicate such carbon is not prone to dissolution in alkaline media. Similar figures for the other two fractions are included in Figure S1.

Figure 2(c) shows data for Ca dissolution. Previous literature results have shown Ca to be minimally soluble in aqueous alkali hydroxide environments,^{48,49} which is confirmed by the observations here. At 6 hours, lime-containing systems appeared oversaturated with Ca. As the systems aged, Ca concentrations quickly diminished, reaching respective solubility limits by 24 hours, and falling to zero at later age. Still, these data, in and of themselves, are not sufficient to conclude the role, or actual consumption of Ca(OH)_2 .

Spectroscopic data presented in Figure 2(d) depict the formation of a new peak at $\sim 970\text{ cm}^{-1}$ coinciding with the disappearance of the sharp peak at $\sim 3640\text{ cm}^{-1}$. 1SL at 72 hours and 0.5SLH at 168 hours of reaction represent fastest and slowest Ca(OH)_2 consumption respectively, as deduced from the transition between regions (1) and (2) in ICP-OES in Figure 2(a). Thus, they are presented in Figure 2(d) to further exemplify the point. Examining the peak at $\sim 3640\text{ cm}^{-1}$ in greater detail, it is clear that while after 72 hours of reaction, there is still ample residual solid Ca(OH)_2 in the 0.5SLH sample, the 1SL sample displays but a blip at that wavenumber. Similarly, after 168 hours of reaction, while there is the faint presence of a peak at $\sim 3640\text{ cm}^{-1}$ for 0.5SLH, it is completely absent from the 1SL system, indicating complete consumption in the 1SL168 system. This agrees with the ICP-OES results. Using these peaks to fingerprint the species present and system evolution in the context of the full spectra and system chemistry, this suggests the precipitation of a calcium silicate hydrate (C-S-H) product as Ca(OH)_2 is consumed.⁵⁰

XRD, FTIR, and NMR data of the 1SL system at multiple time points presented in Figure 3 confirm this conclusion. XRD patterns in Figure 3(a) show the emergence of a broad peak centered at $29^\circ 2\theta$ coinciding with the disappearance of sharp peaks at $18^\circ 2\theta$ and $34^\circ 2\theta$ —features that indicate the formation of a semi-crystalline C-S-H simultaneous with the disappearance of Ca(OH)_2 . As with the pattern shown in Figure 2(b), the patterns presented in

Figure 3(a) display the trend toward decreasing amorphous hump intensity, while maintaining presence of crystalline phases, consistent with literature results.^{30,51} The FTIR series in Figure 3(b) depicts results as explained for 2(c) and are further explained in the supplementary information, with full band assignments presented in Table SI2.

Figure 3(c) shows ²⁹Si MAS-NMR results for raw SA, 168-hour 1SL and 672-hour 1SL samples. The raw SA exhibits a broad, lopsided peak composed of convoluted peaks at -110.4, -101.1, and -88.5 ppm, which are absent from the 1SL672 sample. The spectra for 1SL168 and 1SL672 show development of peaks around -84, -81, and -78 ppm. In terms of silicate network connectivity, these data indicate the destruction of a Q⁴ silicate network with Q³ and Q² sites, reminiscent of the disordered silicate network and associated surface species present in the ash, in exchange for formation Q¹, Q²_b, and Q²_p linkages, as are typically observed in C-S-H.^{40,52} More in-depth analysis of NMR data is presented in the supplementary information, with additional information in Figures SI2 and Table SI3. Mean chain lengths of 5.2-6.5 were calculated according to Equation 1.

$$\text{MCL} = \frac{2(Q^1 + Q_b^2 + Q_p^2)}{Q_1} \quad (1)$$

Such C-S-H precipitation coincident with the dissolution of silica in the presence of Ca(OH)₂ agrees with previous observations,^{33,40,50,52} confirming such reaction schemes upon the use of a non-ideal industrial byproduct, in the form of carbonaceous, mixed-feedstock biomass ash.

4. Discussion

4.1. Byproduct Supply/Utility Prediction

While most academic studies investigate the utility of industrial byproducts through chemical characterization and subsequent synthesis of an alkali activated binder, Bernal, et al. (2016)⁶ points out that they often neglect supply-side analysis. As mentioned, silica-containing agricultural residues such as rice husk and sugarcane bagasse are produced globally at a very large scale (>150 million tons of rice husk and >540 million tons of bagasse annually⁸⁻¹⁰), with cumulative ash content of at least 40 million tons given complete incineration of organic material.¹² While this supply is up to two orders of magnitude smaller than the 4.1 billion tons

of cement produced annually,¹⁹ it represents an opportunity to investigate potential for byproduct use local to its production, thereby offsetting regional demand and offering new solutions engineered with local supply in mind. Still, with variable co-incineration practices and similarly varied efficiencies, it is important to discuss a methodology for estimating chemistry, and therefore utility of ashes similar to the one of focus.

Given appropriate conditions, incineration of rice husk, sugarcane bagasse, and other similar biomass residues is known to produce silica-rich ashes.^{11,53} While these ashes are typically studied in isolation, industrial facilities often burn many feedstocks simultaneously, such as is the practice at Silverton Pulp & Papers Pvt. Ltd. This yields ash with relatively less well-defined chemical and physical properties. Still, where residue inorganic composition is known, it is possible to estimate the contribution of each to the final ash. Silverton-sourced ash used in this study was the result of co-incineration of rice husk (70%) and sugarcane bagasse (30%). According to data assembled by Vassilev, et al. (2010),¹² rice husk and sugarcane bagasse contain approximately 18% and 2% ash (dry-basis), with 94% and 47% of that attributed to SiO_2 , both respectively. Therefore, this ash should theoretically be ~92% SiO_2 . Due to known boiler inefficiencies and discrepancies between reported and real feedstock composition, the ash as received is found to be ~60% SiO_2 with high levels of unburnt organic material. Discounting the contribution of residual unburnt carbon, SiO_2 is calculated to be up to 83% of the ash—almost 10% less than expected, but within reasonable range of the estimate.

4.2. Reactivity/Dissolution of Raw Materials

Still, simple presence of SiO_2 in the precursor material (i.e. biomass ash) does not imply reactivity, necessitating further characterization. Through FTIR, XRD, and ^{29}Si MAS-NMR, shown in Figure 3 above, the ash was determined to be composed primarily of amorphous silica with a variety of minor crystalline phases. Figure 2(a) illustrates that this silica dissolves to varying extent depending on NaOH molarity (and thus, solution pH). These results indicate the glassy silicate network present in the ash dissolves mainly through hydrolysis, following an asymptotic temporal trend.^{28,32,39} As might be expected over the time period considered, while minimal Si was dissolved in water, increasing NaOH molarity, and therefore pH, strongly influenced both Si

extraction extent and rate. Silica solubility is known to be dependent on OH^- concentrations, as it undergoes hydrolysis and forms both silicate anions and Si-O^- surface species.²⁶ Additional studies revealed dissolution dependence on ash concentration (i.e. L/S) and pre-processing of ash to remove organic material. As might be expected, more dilute ash systems (i.e. higher L/S) resulted in faster dissolution of Si due to higher concentration gradients. Removal of carbon with controlled calcination also showed promise as a means of obtaining a more concentrated source of amorphous silica.

Through further analysis of the dissolution results in view of FTIR and NMR spectra, it is clear that hydrolysis-driven dissolution arises from nucleophilic attack at Q^2 - Q^3 sites following by similar reactions at Q^4 sites.²⁶ The lower connectivity Q^2 - Q^3 sites are completely consumed after 7 days of reaction, while Q^4 sites are still observed, in agreement with expected reaction energetics. After 28 days, while crystalline phases are still observed in the XRD pattern, the peaks associated with Q^4 species are no longer readily observed in the NMR spectra, indicating their minimal abundance, also confirmed by XRD, which shows <10% crystalline silicate species.¹⁶ Still, the continued presence of crystalline phases in the XRD patterns is indicative of their resistance to dissolution in the environment as studied, in agreement with literature findings.^{23,51}

4.3. Precipitation of Reaction Products

While dissolution experiments are an important first step for understanding precursor utility (in this case, biomass ash), they can prove more informative when viewed in conjunction with precipitation studies (i.e. in the presence of other reactive materials). Looking back to the SL and SLH samples in Figure 2(a), the initial dormancy in the dissolution trends can be understood as due to the immediate consumption of extracted Si in the presence of $\text{Ca}(\text{OH})_2$, in agreement with observations made previously by Leeman³⁷ and Kim and Olek.³³ The Si apparently reacts as it dissolves until introduced calcium supplies are exhausted, after which the silicon levels in solution are observed to rise in familiar asymptotic fashion. Rather than an actual decrease in dissolution, this represents the precipitation of Si-rich C-S-H species. Grutzeck, et al. (1983)⁵⁴ observed a similar phenomenon when tracking the dissolution of silica fume in saturated

aqueous $\text{Ca}(\text{OH})_2$ solution, noting that Si concentration in solution does not rise with time due to its reaction with the Ca in the presence of water to form a C-S-H type gel. Most recently, Noguchi, et al.³⁵ also observed a decrease in dissolved Si concentration upon glass dissolution in the presence of Ca due to the precipitation of similar products.

This explains the order in which sample Si concentrations rise: 1SL, 1SLH, 0.5SL, 0.5SLH, and is in agreement with the FTIR results shown in Figure 2(d). By comparing 0.5SLH72, 0.5SLH168, 1SL72, and 1SL168, it is evident that both higher molarity NaOH and lower calcium levels lead to faster consumption of $\text{Ca}(\text{OH})_2$. Higher OH^- concentration in 1 M NaOH than 0.5 M NaOH produces a larger driving force for Si dissolution, and therefore, faster consumption of Ca. Furthermore, as the SL samples contain less Ca than SLH samples (i.e. less added $\text{Ca}(\text{OH})_2$), they also demonstrate an earlier rise in apparent Si dissolution.

4.4. Utility of ICP-OES

Upon synthesis of a C-S-H type product, it is necessary to further analyze relevant metrics, such as Ca/Si ratio and alkali adsorption. Here, we suggest that ICP-OES use as described (comparing solution chemistries of standalone dissolution and reaction-prone experiments) can effectively be employed for estimation of such quantities.

For the SA systems, Ca/Si ratios become relevant once it is apparent that all added $\text{Ca}(\text{OH})_2$ has been consumed. FTIR (Figure 2(d)) was useful in clarifying the distinction between dissolution regimes 1 and 2—which, respectively, were defined as flat and asymptotic dissolution in the ICP-OES results of lime-containing systems (Figure 2(a))—and confirmed that once these systems exited regime 1, all added $\text{Ca}(\text{OH})_2$ had been depleted. At the point of transition and thereafter, differences between the S and SL/SLH curves in ICP-OES results could be used to calculate consumed Si, which, in light of complete Ca utilization, could further be used to calculate the Ca/Si of solid SL and SLH products. Such Ca/Si ratios are presented in Table 3.

Generally, as the system evolves, more Si is incorporated into the C-S-H product from solution, yielding a decreasing Ca/Si in the solid product with age. Notably, data for 0.5SL do not explicitly match this trend at all time points included. Furthermore, the calculated Ca/Si for

0.5SLH after 168 hours of reaction is included, even though it is clear from both ICP-OES and FTIR that the $\text{Ca}(\text{OH})_2$ has not been entirely consumed, yielding an elevated Ca/Si estimate.

Given the spectroscopic and diffraction data presented earlier, it is clear that a low calcium, tobermorite-like C-S-H product was synthesized, which agrees with such calculated Ca/Si ratios. Such C-S-H products typically exhibit Ca/Si in the range of 0.6-0.9, similar to those observed here.^{50,52,55-57}

To further verify the accuracy of the calculated ratios, salicylic acid/methanol (SAM) and ethylenediaminetetraacetic acid/sodium hydroxide (EDTA/NaOH) extractions of the solid products were carried out. Extraction experiments were performed on 1SLH samples after 336 hours of reaction, ensuring complete $\text{Ca}(\text{OH})_2$ consumption. While typically used only in association with mass balance for product characterization, extraction solution chemistries were also analyzed by ICP-OES to quantify Ca and Si concentrations extracted from solid products, and thus verify Ca/Si ratios. These techniques are well-documented as useful in dissolving calcium silicate phases.^{22,58-61} Since experiments produced a low-Ca C-S-H phase exhibiting relatively long Si-chains (as identified above), SAM extraction proved to be of only limited use. While SAM extraction resulted in complete removal of Ca from the samples (i.e. removed Ca accounted for all introduced $\text{Ca}(\text{OH})_2$), Si dissolution was severely limited, yielding unreasonable apparent Ca/Si (~ 2.9) from ICP-OES analysis of extraction solution. EDTA/NaOH extraction results, on the other hand, were in agreement with other characterization methods, presenting a Ca/Si ratio of $\sim 0.7-0.8$ from ICP-OES characterization of extraction solution chemistry as well as mass balance. While these results demonstrate the shortcomings of certain selective dissolution techniques as discussed by other authors,^{22,61} they also confirm that the Ca/Si estimates as calculated from ICP-OES and presented in Table 3 are likely accurate. Comparison of Ca/Si values of 1SLH336 samples across all techniques is presented in Table S5.

The authors note that it is still important to take into account the fact that in such systems, heterogeneous surface nucleation of reaction product is known to occur. This phenomenon

could trap otherwise reactive silica species under a newly formed product layer, which would also contribute to the observed depression of Si dissolution. However, in light of the preponderance of evidence, it seems reasonable to the authors that the Ca/Si ratio as calculated from ICP-OES can serve as an accurate estimate.

Similarly, Na adsorption can be calculated based on comparison of starting NaOH solution chemistry with sample filtrate chemistries. As the system evolves, Na incorporation is verified by its relative minimization as compared to stock 0.5 M and 1 M NaOH solutions. After 28 days, Na incorporation was found to be in the range of 1.0-1.8 mmol Na / g solid, as presented in Table 4. Note that the lowest value—1 mmol Na / g solid—corresponds to the highest Ca/Si ratio— ~ 1 , while the higher values—all similar at ~ 1.8 mmol Na / g solid—corresponds to the lower Ca/Si ratios of 0.62-0.74. These values agree with those observed by Hong and Glasser.⁶² For low Ca/Si systems (i.e. Ca/Si = 0.85), Hong and Glasser observed alkali sorption of approximately 1 mmol/g, which matches not only the Na sorption observed in this work, but also the Ca/Si ratio as calculated by ICP-OES results.

5. Conclusions

It is well understood that alkali-activation chemistries rely heavily on precursor solubility and dissolution in alkali-rich solutions.^{28,32,39} In this study, we demonstrated the utility of a multifaceted characterization approach with the ultimate goal of establishing validity of product chemistry estimation via comparison of dissolution and reaction experiments as measured by ICP-OES. While many previous studies have utilized ICP-OES for tracking precursor dissolution in such solutions,^{38,39} few, if any, use the same approach to compare dissolution with elemental uptake to determine product chemistry. This analysis shows that for aqueous dissolution/precipitation reactions, given a well-defined control system, comparison of simple dissolution with results from a system in which product precipitation is known to occur can provide the necessary information to calculate Ca/Si ratio, alkali adsorption, and other relevant chemical metrics. Use of a relatively well-understood reaction chemistry serves as a proof of

concept for this methodology. Future studies on self-reacting materials, such as metakaolin and certain slags, will be conducted to test the efficacy of such an approach.

This work also yields important findings for utility of byproduct-derived precursor materials. As many small- and medium-scale industries throughout the developing world burn silica-rich agricultural residues under conditions yielding ashes similar to that examined, these results have broad impact. Calculation of ash chemistry from feedstock composition yields approximate values, demonstrating a method for chemistry predictions, and allowing industrial plant owners to understand whether ashes can be utilized as for binder precursors. This can deliver decreased landfill burden and production of value-added products in the form of locally-produced construction materials.

6. Acknowledgments

We would like to acknowledge the financial support for this research through the Tata Center for Technology and Design as well as the Environmental Solutions Initiative, both at Massachusetts Institute of Technology (MIT), Cambridge. We also acknowledge support from NSF CAREER #1751925 and partial support of the Government of Portugal through the Portuguese Foundation for International Cooperation in Science, Technology, and Higher Education, through the MIT Portugal Program. The authors thank Mr. Pankaj Agrawal of Bindlas Duplux LTD. (Muzaffarnagar, India) for arranging the procurement of the materials used in this study. This work made use of the MRSEC Shared Experimental Facilities at MIT, supported by the National Science Foundation under award number DMR-1419807. NMR experiments were carried out by Dr. Caitlin Quinn at the University of Delaware NMR Facility. We also acknowledge the research contributions of Josh Dennison, Rachel Osmundsen, Charlie Settens, Timothy McClure, and Wyoming Analytical Laboratories, Inc.

References

1. Worrell E, Price L, Martin N, Hendriks C, Meida LO. Carbon Dioxide Emissions from the Global Cement Industry. *Annu Rev Energy Environ.* 2001;26(1):303–29.
2. Olivier JGJ, Janssens-Maenhout G, Muntean M, Peters JAHW. Trends in global CO₂ emissions: 2016 Report

- [Internet]. PBL Netherlands Environmental Assessment Agency; European Commission, Joint Research Centre. 2016. Available from: http://edgar.jrc.ec.europa.eu/news_docs/jrc-2016-trends-in-global-co2-emissions-2016-report-103425.pdf
3. Davidovits J. Geopolymers: Inorganic polymeric new materials. *J Therm Anal.* 1991;37(8):1633–56.
 4. Provis JL, Bernal SA. Geopolymers and Related Alkali-Activated Materials. *Annu Rev Mater Res.* 2014;44:299–327.
 5. McLellan BC, Williams RP, Lay J, van Riessen A, Corder GD. Costs and carbon emissions for geopolymer pastes in comparison to ordinary portland cement. *J Clean Prod.* 2011;19(9–10):1080–90.
 6. Bernal SA, Rodríguez ED, Kirchheim AP, Provis JL. Management and valorisation of wastes through use in producing alkali-activated cement materials. *J Chem Technol Biotechnol.* 2016;91(9):2365–88.
 7. van Deventer JSJ, Provis JL, Duxson P, Brice DG. Chemical Research and Climate Change as Drivers in the Commercial Adoption of Alkali Activated Materials. *Waste and Biomass Valorization.* 2010;1(1):145–55.
 8. Food and Agriculture Organization of the United Nations. *FAO Rice Market Monitor (RMM)* [Internet]. Vol. XXI. 2018. Available from: www.fao.org/economic/RMM
 9. Silva CC, Melo CA, Soares Junior FH, Moreira AB, Ferreira OP, Bisinoti MC. Effect of the reaction medium on the immobilization of nutrients in hydrochars obtained using sugarcane industry residues. *Bioresour Technol.* 2017;237:213–21.
 10. Champagne ET, Wood DF, Juliano BO, Bechtel DB. The Rice Grain And its Gross Composition. In: *Rice Chemistry and Technology*. Minneapolis, MN: American Association of Cereal Chemists Press; 2004. p. 77–107.
 11. Mengel K, Kirkby EA, Kosegarten H, Appel T. Further Elements of Importance. In: Mengel K, Kirkby EA, Kosegarten H, Appel T, editors. *Principles of Plant Nutrition*. Dordrecht: Springer Netherlands; 2001. p. 639–55.
 12. Vassilev S V., Baxter D, Andersen LK, Vassileva CG. An overview of the chemical composition of biomass. *Fuel.* 2010;89(5):913–33.
 13. Cordeiro GC, Toledo Filho RD, Fairbairn EMR. Effect of calcination temperature on the pozzolanic activity of sugar cane bagasse ash. *Constr Build Mater.* 2009;23(10):3301–3.
 14. James J, Rao MS. Silica from rice husk through thermal decomposition. *Thermochim Acta.* 1986;97(C):329–36.
 15. Hughes E. Biomass cofiring: Economics, policy and opportunities. *Biomass and Bioenergy.* 2000;19(6):457–65.
 16. Chaunsali P, Uvegi H, Osmundsen R, Laracy M, Poinot T, Ochsendorf J, et al. Mineralogical and microstructural characterization of biomass ash binder. *Cem Concr Compos.* 2018;89:41–51.
 17. Kenney KL, Smith WA, Gresham GL, Westover TL. Understanding biomass feedstock variability. *Biofuels.*

- 2013;4(1):111–27.
18. Williams CL, Westover TL, Emerson RM, Tumuluru JS, Li C. Sources of Biomass Feedstock Variability and the Potential Impact on Biofuels Production. *Bioenergy Res.* 2016;9(1):1–14.
 19. Survey USG. Mineral commodity summaries 2019: U.S. Geological Survey. 2019.
 20. Poinot T, Laracy ME, Aponte C, Jennings HM, Ochsendorf JA, Olivetti EA. Beneficial use of boiler ash in alkali-activated bricks. *Resour Conserv Recycl.* 2018;128:1–10.
 21. Chaunsali P, Uvegi H, Traynor B, Olivetti E. Leaching characteristics of biomass ash-based binder in neutral and acidic media. *Cem Concr Compos.* 2019;100:92–8.
 22. Haha M Ben, De Weerd K, Lothenbach B. Quantification of the degree of reaction of fly ash. *Cem Concr Res.* 2010;40(11):1620–9.
 23. Iler RK. *The Chemistry of Silica: Solubility, Polymerization, Colloid and Surface Properties, and Biochemistry.* New York: John Wiley & Sons; 1979.
 24. Okamoto G, Okura T, Goto K. Properties of silica in water. *Geochim Cosmochim Acta.* 1957;12(1–2):123–32.
 25. Roller PS, Ervin, Jr. G. The System Calcium Oxide-Silica-Water at 30°. The Association of Silicate Ion in Dilute Alkaline Solution. *J Am Chem Soc.* 1940;62(3):461–71.
 26. Bunker BC. Molecular mechanisms for corrosion of silica and silicate glasses. *J Non Cryst Solids.* 1994;179(1):300–8.
 27. Schott J, Pokrovsky OS, Oelkers EH. The Link Between Mineral Dissolution/Precipitation Kinetics and Solution Chemistry. *Rev Mineral Geochemistry.* 2009;70(1):207–58.
 28. Oelkers EH, Schott J, Devidal J-L. The effect of aluminum, pH, and chemical affinity on the rates of aluminosilicate dissolution reactions. *Geochim Cosmochim Acta.* 1994;58(9):2011–24.
 29. Snellings R. Solution-Controlled Dissolution of Supplementary Cementitious Material Glasses at pH 13: The Effect of Solution Composition on Glass Dissolution Rates. *J Am Ceram Soc.* 2013;96(8):2467–75.
 30. Oey T, Kumar A, Pignatelli I, Yu Y, Neithalath N, Bullard JW, et al. Topological controls on the dissolution kinetics of glassy aluminosilicates. *J Am Ceram Soc.* 2017;100(12):5521–7.
 31. Hamilton JP, Brantley SL, Pantano CG, Criscenti LJ, Kubicki JD. Dissolution of nepheline, jadeite and albite glasses: toward better models for aluminosilicate dissolution. *Geochim Cosmochim Acta.* 2001;65(21):3683–702.
 32. Newlands KC, Foss M, Matchei T, Skibsted J, Macphee DE. Early stage dissolution characteristics of aluminosilicate glasses with blast furnace slag- and fly-ash-like compositions. *J Am Ceram Soc.* 2017;100(5):1941–55.
 33. Kim T, Olek J. Chemical Sequence and Kinetics of Alkali-Silica Reaction Part I. Experiments. *J Am Ceram Soc.*

- 2014;97(7):2195–203.
34. Maraghechi H, Rajabipour F, Pantano CG, Burgos WD. Effect of calcium on dissolution and precipitation reactions of amorphous silica at high alkalinity. *Cem Concr Res.* 2016;87:1–13.
 35. Noguchi N, Morinaga Y, Kajio T, Yogarajah E, Nawa T. Influence of portlandite on Pyrex glass dissolution and the formation of alkali-silica chemical reaction products. *J Am Ceram Soc.* 2018;101(10):4549–59.
 36. Bulteel D, Garcia-Diaz E, Vernet C, Zanni H. Alkali–silica reaction: A method to quantify the reaction degree. *Cem Concr Res.* 2002;32(8):1199–206.
 37. Leemann A, Le Saout G, Winnefeld F, Rentsch D, Lothenbach B. Alkali-Silica Reaction: the Influence of Calcium on Silica Dissolution and the Formation of Reaction Products. *J Am Ceram Soc.* 2011;94(4):1243–9.
 38. Xu H, Van Deventer JSJ. The geopolymerisation of alumino-silicate minerals. *Int J Miner Process.* 2000;59(3):247–66.
 39. Hajimohammadi A, van Deventer JSJ. Dissolution behaviour of source materials for synthesis of geopolymer binders: A kinetic approach. *Int J Miner Process.* 2016;153:80–6.
 40. Abreu RF, Schneider J, Cincotto MA. Structure and Hydration Kinetics of Silica Particles in Rice Husk Ash Studied by ²⁹Si High-Resolution Nuclear Magnetic Resonance. *J Am Ceram Soc.* 2005;88(6):1514–20.
 41. Heo UH, Sankar K, Kriven WM, Musil SS. Rice Husk Ash as a Silica Source in a Geopolymer Formulation. In: Kriven WM, Zhu D, Moon K IL, Hwang T, Wang J, Lewinsohn C, et al., editors. *Developments in Strategic Materials and Computational Design V: A Collection of Papers Presented at the 38th International Conference on Advanced Ceramics and Composites.* NJ, USA: John Wiley & Sons, Inc.; 2015. p. 87–102.
 42. Biernacki JJ, Williams PJ, Stutzman PE. Kinetics of Reaction of Calcium Hydroxide and Fly Ash. *ACI Mater J.* 2001;98(4):340–9.
 43. Mohebbi M, Rajabipour F, Scheetz BE. Evaluation of Two-Atmosphere Thermogravimetric Analysis for Determining the Unburned Carbon Content in Fly Ash. *Adv Civ Eng Mater.* 2017;6(1):20160052.
 44. Greenberg SA. The Depolymerization of Silica in Sodium Hydroxide Solutions. *J Phys Chem.* 1957;61(7):960–5.
 45. Alexander GB, Heston WM, Iler RK. The Solubility of Amorphous Silica in Water. *J Phys Chem.* 1954;58(6):453–5.
 46. Saenko NS. The X-ray diffraction study of three-dimensional disordered network of nanographites: Experiment and theory. *Phys Procedia.* 2012;23(2011):102–5.
 47. Bouzón N, Payá J, Borrachero MV, Soriano L, Tashima MM, Monzó J. Refluxed rice husk ash/NaOH suspension for preparing alkali activated binders. *Mater Lett.* 2014;115:72–4.
 48. Pallagi A, Tasi Á, Gácsi A, Csáti M, Pálinkó I, Peintler G, et al. The solubility of Ca(OH)₂ in extremely concentrated NaOH solutions at 25°C. *Cent Eur J Chem.* 2012;10(2):332–7.

49. Konno H, Nanri Y, Kitamura M. Crystallization of aragonite in the causticizing reaction. *Powder Technol.* 2002;123(1):33–9.
50. Yu P, Kirkpatrick RJ, Poe B, McMillan PF, Cong X. Structure of Calcium Silicate Hydrate (C-S-H): Near-, Mid-, and Far-Infrared Spectroscopy. *J Am Ceram Soc.* 1999;82(3):742–8.
51. Pignatelli I, Kumar A, Bauchy M, Sant G. Topological Control on Silicates' Dissolution Kinetics. *Langmuir.* 2016;32(18):4434–9.
52. Cong X, Kirkpatrick RJ. ²⁹Si MAS NMR Study of the Structure of Calcium Silicate Hydrate. *Adv Cem Based Mater.* 1996;3(3–4):144–56.
53. Vassilev S V, Baxter D, Andersen LK, Vassileva CG. An overview of the composition and application of biomass ash. Part 1. Phase-mineral and chemical composition and classification. *Fuel.* 2013;105:40–76.
54. Grutzeck MW, Atkinson S, Roy DM. Mechanism of Hydration of Condensed Silica Fume in Calcium Hydroxide Solutions. *ACI Spec Publ.* 1983;SP-79(2):643–64.
55. Richardson IG. The calcium silicate hydrates. *Cem Concr Res.* 2008;38(2):137–58.
56. Taylor HFW. *Cement chemistry.* Acad Press. 1997;475:683–93.
57. Kirkpatrick RJ, Yarger JL, McMillan PF, Yu P, Cong X. Raman Spectroscopy of C-S-H, Tobermorite, and Jennite. *Adv Cem Based Mater.* 1997;5(3–4):93–9.
58. García Lodeiro I, Macphee DE, Palomo A, Fernández-Jiménez A. Effect of alkalis on fresh C–S–H gels. FTIR analysis. *Cem Concr Res.* 2009;39(3):147–53.
59. Puligilla S, Mondal P. Co-existence of aluminosilicate and calcium silicate gel characterized through selective dissolution and FTIR spectral subtraction. *Cem Concr Res.* 2015;70:39–49.
60. Chen X, Sutrisno A, Struble LJ. Effects of calcium on setting mechanism of metakaolin-based geopolymer. *J Am Ceram Soc.* 2018;101(2):957–68.
61. Luke K, Glasser FP. Selective dissolution of hydrated blast furnace slag cements. *Cem Concr Res.* 1987;17(2):273–82.
62. Hong S-Y, Glasser FP. Alkali binding in cement pastes: Part I. The C-S-H phase. *Cem Concr Res.* 1999;29(12):1893–903.

Figure Captions:

Figure 1. (a) XRD pattern of raw biomass ash (<500 μm) sourced from Silverton Pulp & Papers Pvt. Ltd. (b) XRD patterns of ash fraction: <45 μm , 45-150 μm , and 150-500 μm

Figure 2. (a) Extent of Si dissolution from SA as a function of time at L/S of 25. 0S, 0.5S, and 1S fit asymptotically with solid lines. SL and SLH sample data fit qualitatively for two regions (dotted lines): (1) apparently flat dissolution (reaction) followed by (2) asymptotic dissolution. (b) Normalized XRD patterns of SA particles 150-500 μm in size before and after 672 hours (28 days) of dissolution. (c) Concentration of Ca (millimolarity) in aqueous 0.5 M and 1 M NaOH systems as a function of time. Dotted lines denote literature values for Ca solubility in such solutions. (d) Normalized FTIR absorbance spectra of four samples for comparison of $\text{Ca}(\text{OH})_2$ consumption (peak at $\sim 3640\text{ cm}^{-1}$) with C-S-H production (peak at $\sim 970\text{ cm}^{-1}$).

Figure 3. (a) XRD results showing system evolution with time. Note: diminution of portlandite peaks ($\text{Ca}(\text{OH})_2$), evolution of C-S-H peak (specifically associated with Tobermorite-like phase), and decrease in intensity of amorphous hump. (b) Normalized FTIR absorbance spectra of Silverton ash, 6 hour, 24 hour, 72 hour, 168 hour, and 672 hour samples of ash dissolved in 1 M NaOH in the presence of $\text{Ca}(\text{OH})_2$ at an ash/lime ratio of 87.5/12.5. (c) ^{29}Si MAS-NMR of raw Silverton ash, 1SL168, and 1SL672 along with their deconvolution into Gaussian curves (in gray) and sum of the separate curves (in red) stacked for comparison. Referenced externally to hexamethylcyclotrisiloxane at -9.00 ppm.

Tables and Captions:

Table 1 Average chemical composition (oxide %) of four SA samples using XRF. Uncertainty represents one standard deviation.

Oxide (%)	SiO_2	Al_2O_3	Fe_2O_3	Na_2O	K_2O	CaO	MgO	P_2O_5	SO_3	Trace*	LOI [#]	Amorphous Content [†]
Biomass	61.2	1.6	0.69	0.22	2.5	1.59	0.80	0.91	1.89	0.19	28.4	90%
Ash	± 1.2	± 0.5	± 0.09	± 0.08	± 0.3	± 0.09	± 0.07	± 0.07	± 0.13	± 0.05	± 1.5	

* Includes TiO_2 , MnO_2 , BaO, and SrO; [#] loss-on-ignition (LOI) at 750 °C; [†]As determined by Rietveld XRD – includes contribution from unburnt carbon

Table 2 Sample identification. Liquid/Solid ratio for all samples = 25.

Sample ID	Age (hrs)	NaOH (M)	Silverton Ash (wt%)	$\text{Ca}(\text{OH})_2$ (wt%)
0Sx	x	0	100	0
0SLx	x	0	87.5	12.5
0SLHx	x	0	82.5	17.5
0.5Sx	x	0.5	100	0

0.5SLx	x	0.5	87.5	12.5
0.5SLHx	x	0.5	82.5	17.5
1Sx	x	1	100	0
1SLx	x	1	87.5	12.5
1SLHx	x	1	82.5	17.5

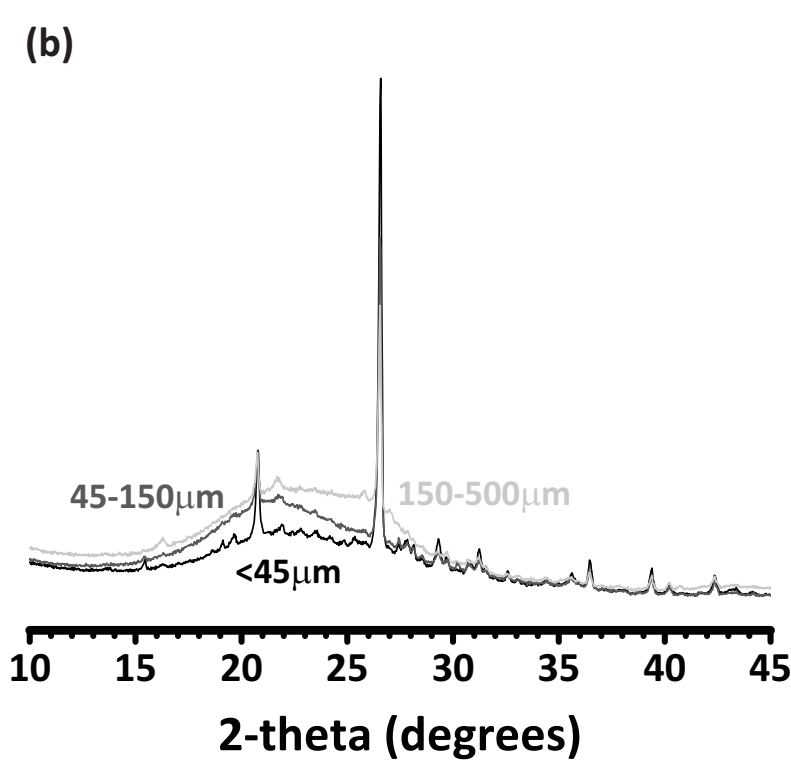
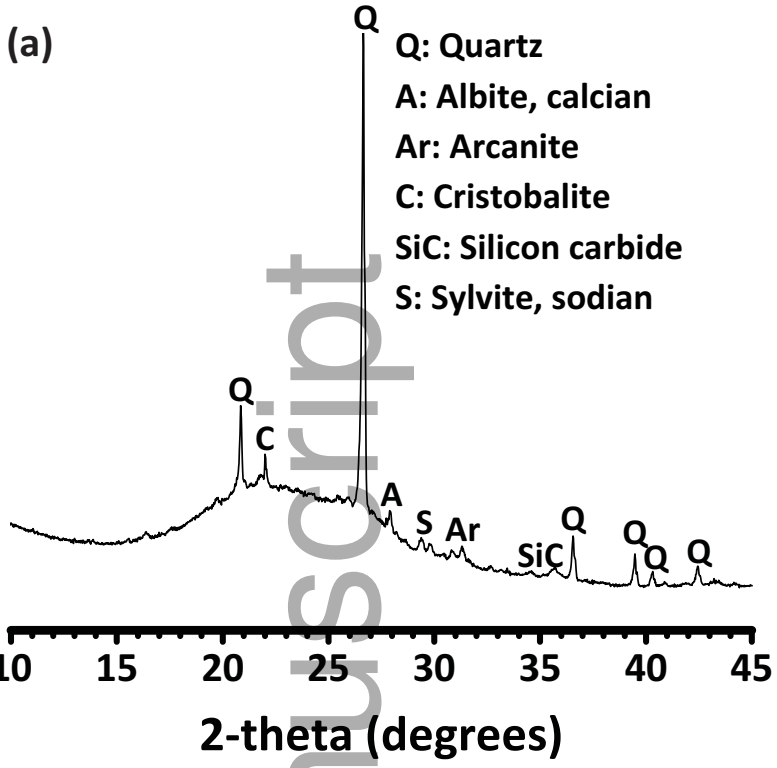
Table 3. Ca/Si ratios of solid SL and SLH products as calculated from ICP-OES results at 7, 14, and 28 days.

Uncertainty represents 95% confidence interval when calculating differences in Si levels between ash dissolution and reaction with horizontal and vertical aggregation analysis.

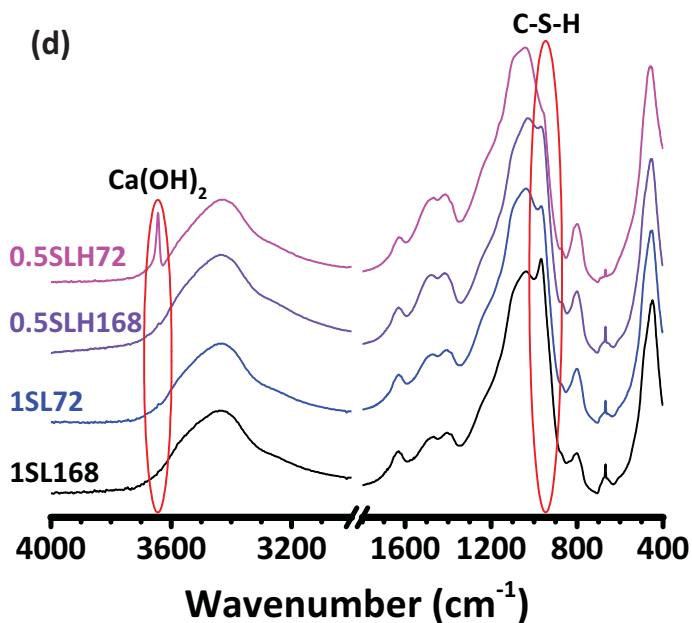
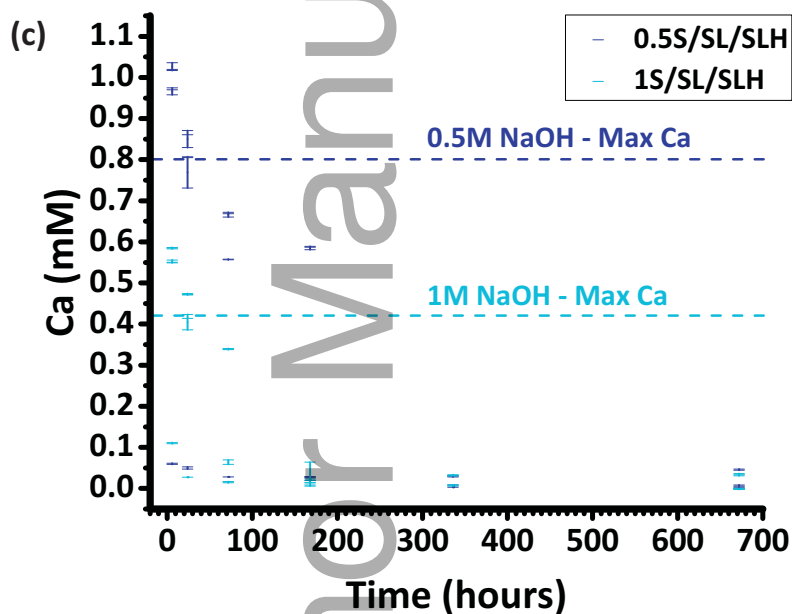
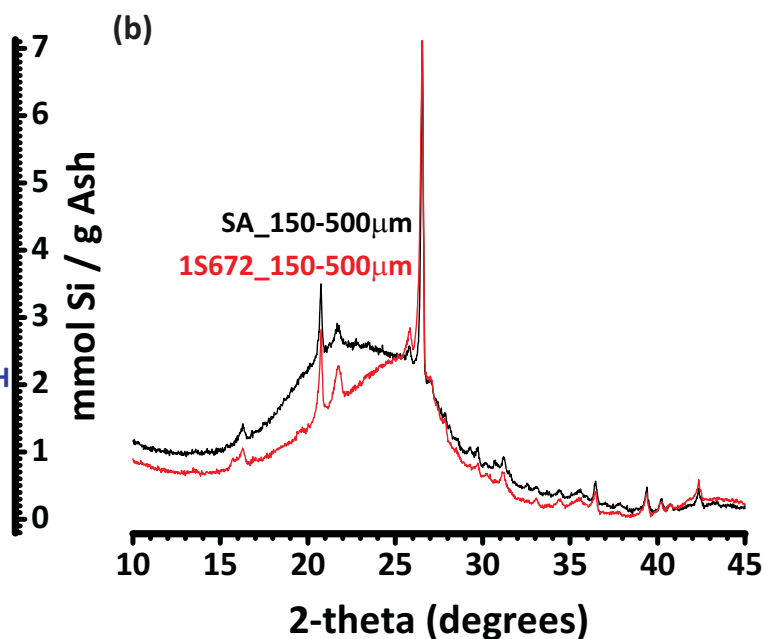
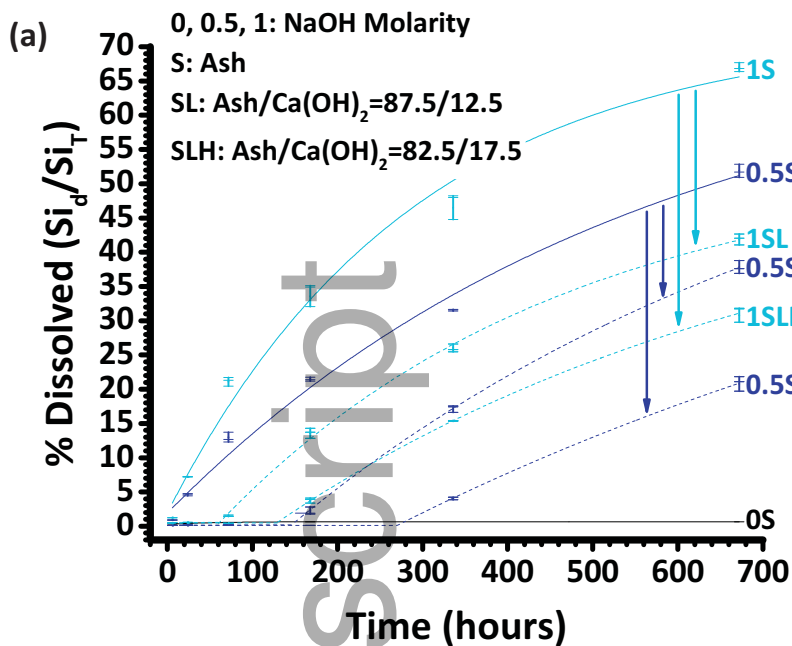
Ca/Si				
Time (hours)	0.5SL	0.5SLH	1SL	1SLH
168	0.98±0.03	1.20±0.02	0.85±0.01	0.82±0.01
336	1.18±0.06	0.91±0.03	0.85±0.02	0.78±0.01
672	1.01±0.04	0.74±0.02	0.63±0.01	0.62±0.01

Table 4. Na adsorption after 672 hours of sample evolution, in mmol Na/g solid.

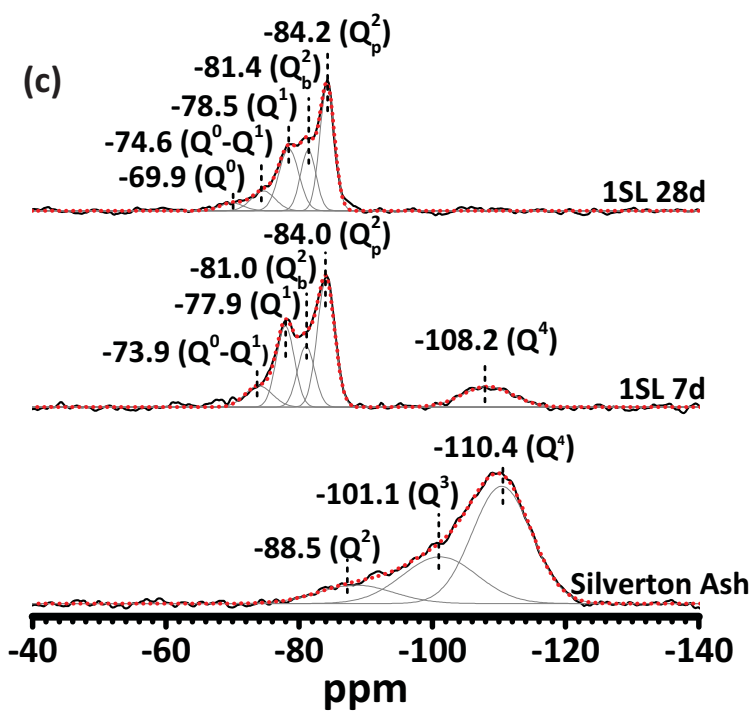
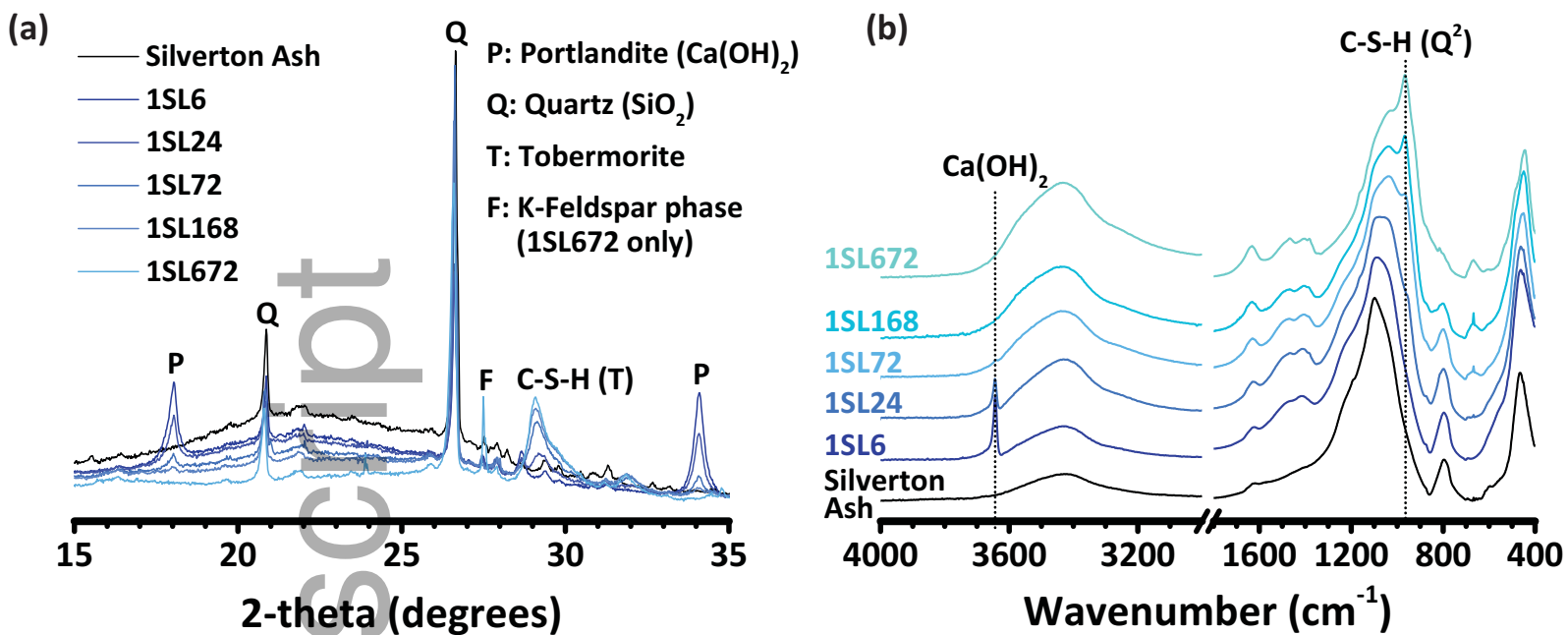
Na adsorption (mmol Na / g solid)				
Time (hours)	0.5SL	0.5SLH	1SL	1SLH
672	1.0±0.3	1.8±0.3	1.7±0.2	1.8±0.1



jace_16628_f1.eps



jace_16628_f2.eps



jace_16628_f3.eps